ADVANCED ENERGY MATERIALS
www.advenergymat.de

Locally Supersaturated Inks for a Slot-Die Process to Enable Highly Efficient and Robust Perovskite Solar Cells

Sushil S. Sangale, Sung-Nam Kwon, Pramila Patil, Hyun-Jung Lee, and Seok-In Na**

Perovskite solar cells (PSCs), which debuted with a lot of attention based on high efficiency, are establishing as one of the most promising thin-film photovoltaic technologies. Currently, research for upscaling and commercialization through eco-friendly solvent and process systems is being attempted. This study introduces for the first time a rheological engineering-based locally supersaturated perovskite ink (LSPI) strategy for slot-die process-based PSC fabrication suitable for roll-to-roll continuous processes. Here, for the greenable slot-die process, a perovskite precursor ink composed of a low-toxic dimethyl sulfoxide (DMSO) single solvent is used and a small amount of 1,2-dichlorobenzene (DCB) is utilized as a modulator to control the rheological properties of the ink. The addition of DCB lowers the high surface tension of the DMSO-based perovskite precursor ink to suit the slot-die process, enabling uniform wet film formation, and produces locally supersaturated colloids, i.e., perovskite seeds, that help growth into dense and large grains by heterogeneous nucleation with low Gibbs-free energy. As a result, the LSPI enables slot-die coating-based PSCs with an efficiency of 20.61% (active areas of 0.1 cm^2), which allow high efficiencies of 18.66% and 17.66% (active areas of 2.7 and 8.64 cm^2) to be achieved in scale-up to minimodules, respectively.

1. Introduction

Perovskite solar cells (PSCs) have attracted enormous attention in the past decade due to their excellent photovoltaic properties, and their power conversion efficiency (PCE) has reached 25.7% at a very fast rate in a short period of time.[1] Currently, PSCs are establishing as one of the most promising thin-film photovoltaic (PV) technologies, and research is being attempted for upscaling and commercialization. For the commercialization of PSCs, it is necessary to manufacture large-area PSCs through eco-friendly solvents and processes. This is because large amounts of highly toxic solvent vapors such as dimethylformamide (DMF), commonly used as the main solvent for high-efficiency PSCs, may be released during the perovskite film formation process, which can be dangerous to both people and the environment.[2] To replace or reduce the content of toxic solvents (e.g., DMF, γ-butyrolactone, N-methyl-2-pyrrolidone, 2-methoxyethanol, acetonitrile, etc.), less toxic solvents such as dimethyl sulfoxide (DMSO), ethanol, methylammonium acetate, and tetrahydrofuran have been utilized.[2,3] However, the use of solvents with low toxicity makes it difficult to form high-quality perovskite thin film, and the resulting low efficiency is insufficient to be competitive for commercialization.[4] Therefore, the development of a perovskite precursor ink using an eco-friendly solvent and technology for realizing a high-quality perovskite thin film using it is a key issue for mass production and commercialization of perovskite solar cells.

Currently, multicationic perovskites based on cesium (Cs), formamidenium (FA), and methylammonium (MA) are mainly used to improve the efficiency and stability of PSCs, but there is a limit to the selection of solvents that can simultaneously dissolve Pb precursors (e.g., PbI_2, $PbBr_2$, etc.) and Cs precursors (e.g., CsI_2, $CsBr_2$, etc.) while maintaining environmental friendliness. In this respect, DMSO, a commonly used aprotic organic solvent, can be the best choice for multicationic perovskites and environmental friendliness; DMSO is one of the most environmentally friendly and least toxic solvents that can dissolve perovskite precursors.[3a,5] However, using a single DMSO solvent for perovskite precursors is a challenge. The high surface tension (42.8 mN m^{-1}) and high viscosity (2.0 cP) of DMSO, which is higher than DMF, GBL, NMP or mixed solvents thereof, reduce the wettability of perovskite precursor and consequently lead to nonuniform and low-quality perovskite thin films.[6] Moreover, the lower vapor pressure (8.18×10^{-4} atm at 25 °C) and higher boiling point (189 °C) of DMSO require long solvent evaporation times at low temperatures, which make complex quenching and increase processing time for perovskite film formation.[7] With these issues, pure DMSO-based PSCs still show relatively low efficiency.[4,6a,b]

Importantly, the rheological properties of the perovskite precursor ink have a more profound effect on the large-area solar cell manufacturing process, including spray coating,[8] blade coating,[6d] ink-jet printing,[9] roll-to-roll printing,[10]

S. S. Sangale, S.-N. Kwon, P. Patil, H.-J. Lee, S.-I. Na
Department of Flexible and Printable Electronics and LANL-JBNU Engineering Institute-Korea
Jeonbuk National University
567, Baekje-daero, Deokjin-gu, Jeonju-si, Jeollabuk-do 54896, Republic of Korea
E-mail: dasom2u@jbnu.ac.kr; nsi12@jbnu.ac.kr

The ORCID identification number(s) for the author(s) of this article can be found under https://doi.org/10.1002/aenm.202300537

DOI: 10.1002/aenm.202300537

industrial-based slot-die coating.[6b,11] Among them, slot-die coating is one of the most promising technologies for PSC manufacturing that has already been proven in the industrial field, and slot-die coating-based PSC is showing continuous progress along with N_2 blowing, additives, and antisolvent bathing technologies.[12] However, the absence of a perovskite precursor ink suitable for slot-die coating makes it difficult to implement high-quality perovskite thin films and achieve high efficiency. Meanwhile, the quality of the slot-die coated thin film is determined by parameters such as coating speed, coating interval, flow rate, surface tension, and viscosity of the ink, and the rheological properties of the ink, including surface tension and viscosity, are key variables for the formation of the initial uniform wet film by slot-die coating.[13] For instance, a very small amount of surfactant (l-α-phosphatidylcholine) dramatically altered the fluid drying kinetics, increased the adhesion of the perovskite ink to the underlying nonwetting charge transport layer, and enabled the blading of smooth perovskite films, achieving efficiencies in excess of 20%.[14] In addition, the viscosity of the perovskite ink was controlled by adding acetonitrile (ACN) to the 2-methoxyethanol-based formamidinium lead triiodide ($FAPbI_3$) precursor ink, consequently, a slot-die-based smooth perovskite film with no ribbing effects and a minimodules (12.7 cm^2) with a PCE of 17.1% was achieved.[15] Further, the volatile cosolvent mixed to dilute the perovskite precursor ink to a low concentration (<0.5 M) allowed it to maintain film quality and optoelectronic properties similar to those of the high concentration precursor (>1.4 M), resulting in a high module efficiency of over 18%.[2a] Thus, the rheological properties of the perovskite precursor ink are critical to the formation of perovskite thin films that crystallize from wet films through a process of nucleation and growth.[16] From this point of view, there have been reports of studying the rheological properties of perovskite precursor inks, but unfortunately all these reports are based on the use of toxic perovskite solvent systems, which still raises concerns about the application of scaling-up processes for commercialization.

In this study, we report an advanced strategy for perovskite precursor inks based on low-toxic solvents and suitable for scale-up processes such as slot-die coating. For the first time, we demonstrate that the addition of a small amount of 1,2-dichlorobenzene (DCB), to DMSO-based triple cation perovskite precursor inks can modulate the rheology of ink and improve the formation of the perovskite thin film through the slot-die process. The addition of a small amount of DCB lowered the surface tension and viscosity of the DMSO-based perovskite precursor ink and at the same time formed locally supersaturated perovskite colloids, i.e., perovskite seeds. This strategy allowed to coat a uniform perovskite thin film and to fabricate a PSC with a p–i–n architecture with an active area of 0.1 cm^2 and an efficiency of 20.61% through a slot-die coating process. Furthermore, the slot-die coated minimodules with active areas of 2.7 and 8.64 cm^2 achieved PCE of 18.66% and 17.66%, respectively. The unencapsulated small device retained >85% PCE for more than 4320 h in a nitrogen glove box, while the minimodule retained >83% PCE for more than 1920 h. Our results pave the way to fabricate highly efficient and robust PSCs via greenable perovskite precursor inks and slot-die process, an important step toward the commercialization of PSCs.

2. Results and Discussion

2.1. DMSO-Based Perovskite Precursor Ink

Among the various solvents used in perovskite solar cells, DMSO was selected as a greener solvent that can be used in consideration of solubility and toxicity (Table S1, Supporting Information), and conventional perovskite precursor inks based on triple cations were prepared with 100% DMSO solvent (denoted as conventional perovskite ink; CPI). The DMSO solvent showed excellent solubility within the commonly used perovskite precursor content range of 1.1–1.5 M (Figure S1, Supporting Information) and considering the coating properties of the ink and the quality of the thin film, an ink containing 1.4 M perovskite precursors was selected as the optimal condition for subsequent experiments. Subsequently, the designed modulating-solvent DCB was introduced into the as-prepared conventional perovskite precursor ink to prepare a locally supersaturated perovskite precursor ink (denoted as locally supersaturated perovskite ink; LSPI). Detailed experimental procedures for perovskite precursor inks can be found in the Supporting Information. Here, considering the solubility and rheological properties of the perovskite precursor ink, DCB was selected as an example of a modulating-solvent to demonstrate the concept in this work with the following rationale: i) easily miscible with existing solvent (DMSO), ii) low surface tension and low viscosity (improves wettability to help form a wet film),[17] iii) similar boiling point and higher vapor pressure to existing solvents (does not create bubbles and requires less energy and time to dry),[17a] iv) low dipole moment and no interaction with perovskite precursors (lowering the solubility without coordination bonding with the perovskite precursor). Table S2 of the Supporting Information shows the solution properties of antisolvent including DCB and **Figure 1** presents the schematic concept of the locally supersaturated perovskite ink. The addition of DCB to perovskite precursor inks is expected to miscible with DMSO solvent to reduce the surface tension and viscosity of the ink, while reducing local solubility by antisolvent action, leading to supersaturation and perovskite colloid formation, i.e., perovskite seed.

To prove the concept of locally supersaturated perovskite inks, we systematically investigated the physicochemical properties of triple-cation perovskite precursor inks containing DCB. As a control, CPI, a conventionally prepared perovskite precursor ink, was prepared by dissolving the triple-cation perovskite precursor ($Cs_{0.05}(FA_{0.92}MA_{0.08})_{0.95}Pb$-$(I_{0.92}Br_{0.08})_3$) in 100% DMSO at a concentration of 1.4 M. As a target, LSPI, a locally supersaturated perovskite precursor ink, was prepared by adding different volume ratios of DCB (5 to 30 vol%) to as-prepared CPI (**Figure 2**a). The added DCB did not exhibit any chemical interaction with the perovskite precursor as well as DMSO in Fourier-transform infrared spectroscopy analysis (Figure S2, Supporting Information). However, over time, in the inks with 20 and 30 vol% DCB added, precipitates were formed after 12 and 3 h, respectively, due to the antisolvent action by the excessive amount of DCB (Figure S3, Supporting Information). On the other hand, when DCB was added at 15 vol% or less, transparent ink was maintained without precipitation for more than 24 h. Therefore, despite being an antisolvent, it can be seen that when an appropriate amount of DCB is added to the perovskite precursor solution, it can be well

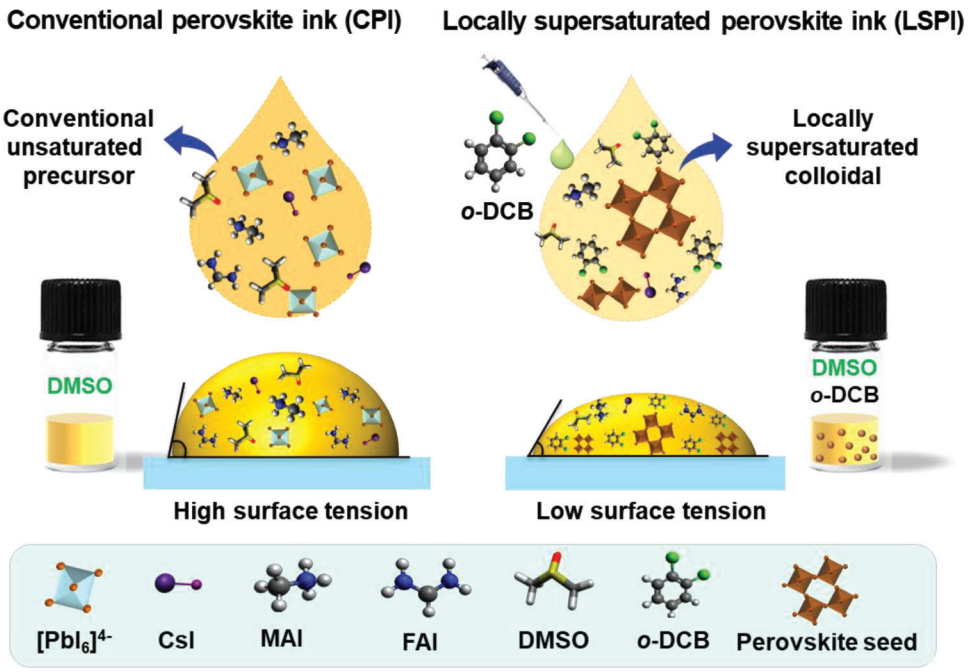

Figure 1. Schematic illustration of the locally supersaturated perovskite precursor inks. The top part of the panel: locally supersaturation process of perovskite precursor ink using DCB antisolvent as a modulator. The bottom part of the panel: chemical compounds used in the perovskite ink and their structures.

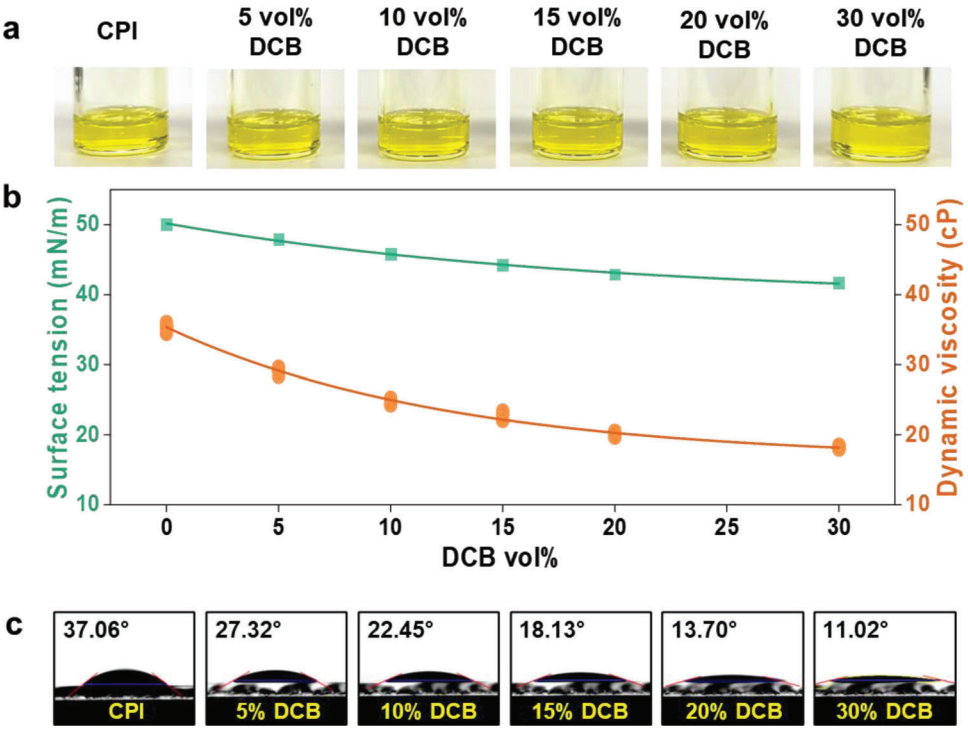

Figure 2. Physicochemical properties of LSPI. a) Photograph of CPI and LSPI with various concentrations of DCB. b) Changes in surface tension and dynamic viscosity of perovskite precursor inks with different DCB contents. c) Contact angles of the corresponding perovskite precursor ink with different DCB contents measured on the NiO-coated ITO substrate.

mixed with DMSO and the perovskite precursor, allowing the ink to maintain a stable state.

To further examine the changes in the rheological properties of perovskite precursor inks following the addition of DCB, the surface tension (σ) and dynamic viscosity (η) of CPI and LSPI were measured. As the addition amount of DCB increased from 0 to 30 vol%, the σ of the LSPI gradually decreased from 50.04 to 41.73 mN m^{-1}, and at the same time, the η decreased from 35.38 to 18.20 cP (Figure 2b). This means that as the addition amount of DCB (σ of 35.0 mN m^{-1} and η of 1.32 cP) increases, σ and η of the perovskite precursor ink decrease and wet film formation can be improved. The contact angles of the corresponding perovskite precursor ink measured on the NiO-coated ITO substrate showed an analogous trend with the σ and η (Figure 2c). With the addition of DCB, the contact angle was lowered from 37.06° to 11.02°, and a more uniform and thicker film was formed (Figure S4, Supporting Information). Evidently, the quality of thin films coated with DMSO-based perovskite precursor inks was improved by the addition of DCB, because the rheological properties and wettability of the ink were improved with the addition of DCB with low surface tension and viscosity. This may additionally be attributed to the formation of local supersaturation and perovskite colloids following the addition of DCB having antisolvent properties, which will be described in detail below in Section 2.2.

2.2. Mechanism of Locally Supersaturated Perovskite Ink

We speculate that when DCB is added to the CPI, the solubility of the perovskite precursor ink decreases and local supersaturation occurs, eventually leading to the formation of perovskite colloids, that is, perovskite seeds. To confirm our hypotheses and mechanisms for the LSPI, dynamic light scattering (DLS) measurements were performed on the ink. Surprisingly, contrary to expectations, it was observed that colloidal phases, which are divided into small and large diameters, were formed in the inks not only in LSPI but also in CPI (**Figure 3**a). In DLS, CPI showed the formation of colloidal phases with an average diameter of 2 and 2445 nm, while LSPI showed the formation of a colloidal phase with an average diameter of 3 and 3435 nm. In particular, with the addition of DCB, the proportion of colloidal phases with diameters from ≈1200 to ≈9000 nm increased significantly compared to CPI. These results mean that the diameter of the colloid increased with the addition of DCB, and considering that the scattering and total absorption of light passing through the ink containing a lot of large-sized colloids increase, the increase in UV–vis absorption is well consistent with this as one evidence for more colloid formation and an increase in colloidal diameter (Figure S5, Supporting Information).[18] Here, the density and size of the colloidal phase have a close and profound effect on nucleation and growth, and the theory of nucleation and growth can be used to predict the formation process of perovskite crystals and thin film formation. Crystallization of perovskite follows the classical nucleation and growth theory, and nucleation and growth are the two main processes of perovskite thin film formation.[19] When the solution concentration reaches a critical concentration and becomes supersaturated, the perovskite solution starts to nucleate and external thermal energy helps it grow into crystals. For example, antisolvent treatment can serve as a trigger to reach supersaturation and initiate nucleation,[20] and in this study, the antisolvent, DCB, created local supersaturation and produced coarse colloids favoring crystallization. The kinetics of perovskite crystallization can be understood through the Gibbs free energy change (ΔG) for nucleation. Based on the classical nucleation theory, ΔG for the perovskite nucleation can be described using Equation (1)[20]

$$\Delta G\ (r) = \Delta G_{\mathrm{V}} + \Delta G_{\mathrm{S}} = \left(-\frac{4}{3V_{\mathrm{M}}}\pi r^3\right)\ RT\ln\left(\frac{C}{C_0}\right) + 4\pi r^2\gamma \quad (1)$$

where r denotes the radius of the nucleus, ΔG_{V} denotes the volume term of the free energy, ΔG_{S} denotes the surface free energy, V_{M} denotes the volume of the nucleus, R denotes the gas constant, T denotes the absolute temperature, C denotes concentration, C_0 denotes the concentration limit, and γ denotes the interfacial tension. In our case, coarse colloids can be considered as nuclei that induce heterogeneous nucleation,[20] and the increase in V_{M} in Equation (1) can reduce ΔG_{V} and consequently significantly reduce the overall energy barrier (ΔG_{Het}) for nucleation (Figure 3b). Meanwhile, the perovskite crystal formation process may have homogeneous or heterogeneous nucleation kinetics, which can be determined through the contact angle (θ) of the perovskite ink according to the following equation[21]

$$\Delta G_{\mathrm{Heterogeneous}} = \Delta G_{\mathrm{Homogeneous}} * f\ (\theta) \quad (2)$$

where

$$f\ (\theta) = \frac{(2+\cos\theta)\,(1-\cos\theta)^2}{4} \quad (3)$$

The free energy required for heterogeneous nucleation (ΔG_{Het}) can be expressed as a function of the free energy required for homogeneous nucleation (ΔG_{Hom}) and the contact angle. In case of $\theta = 180°$, i.e., $f(\theta) = 1$, there is no wettability, and the perovskite crystallization process follows homogeneous nucleation ($\Delta G_{\mathrm{Het}} = \Delta G_{\mathrm{Hom}}$). However, in case of $0° \le \theta \le 180°$, i.e., $0 \le f(\theta) \le 1$, the barrier energy required for heterogeneous nucleation decreases with decreasing contact angle ($\Delta G_{\mathrm{Het}} \le \Delta G_{\mathrm{Hom}}$). From this relationship, it can be seen that heterogeneous nucleation occurs in LSPI with DCB, and the barrier energy required for heterogeneous nucleation decreases with increasing amounts of DCB addition (refer to the change in contact angle in Figure 2c). Accordingly, both CPI and LSPI follow heterogeneous nucleation in perovskite crystallization, but the nucleation energy of LSPI with coarse perovskite colloids and low contact angles is lower, which is favorable for the formation of high-quality perovskite films with uniform and low defects.

X-ray diffraction (XRD) spectroscopy was performed to demonstrate perovskite crystallization with heterogeneous nucleation (Figure 3c). In the XRD pattern of the CPI-based thin film that was not annealed after coating, characteristic peaks indicating the formation of a small amount of perovskite seeds ($2\theta = 23.5°$ and 34.8°) together with the typical DMSO-PbI_2 phase ($2\theta = 12.2°$ and 25.6°) were observed,[22] which is consistent with the formation of small and large colloidal phases observed through DLS analysis in Figure 3a. Further, obviously, the XRD patterns of the LSPI-based thin films showed a characteristic peak of stronger perovskite seeds ($2\theta = 14.6°$, 24.1°, and 34.8°)

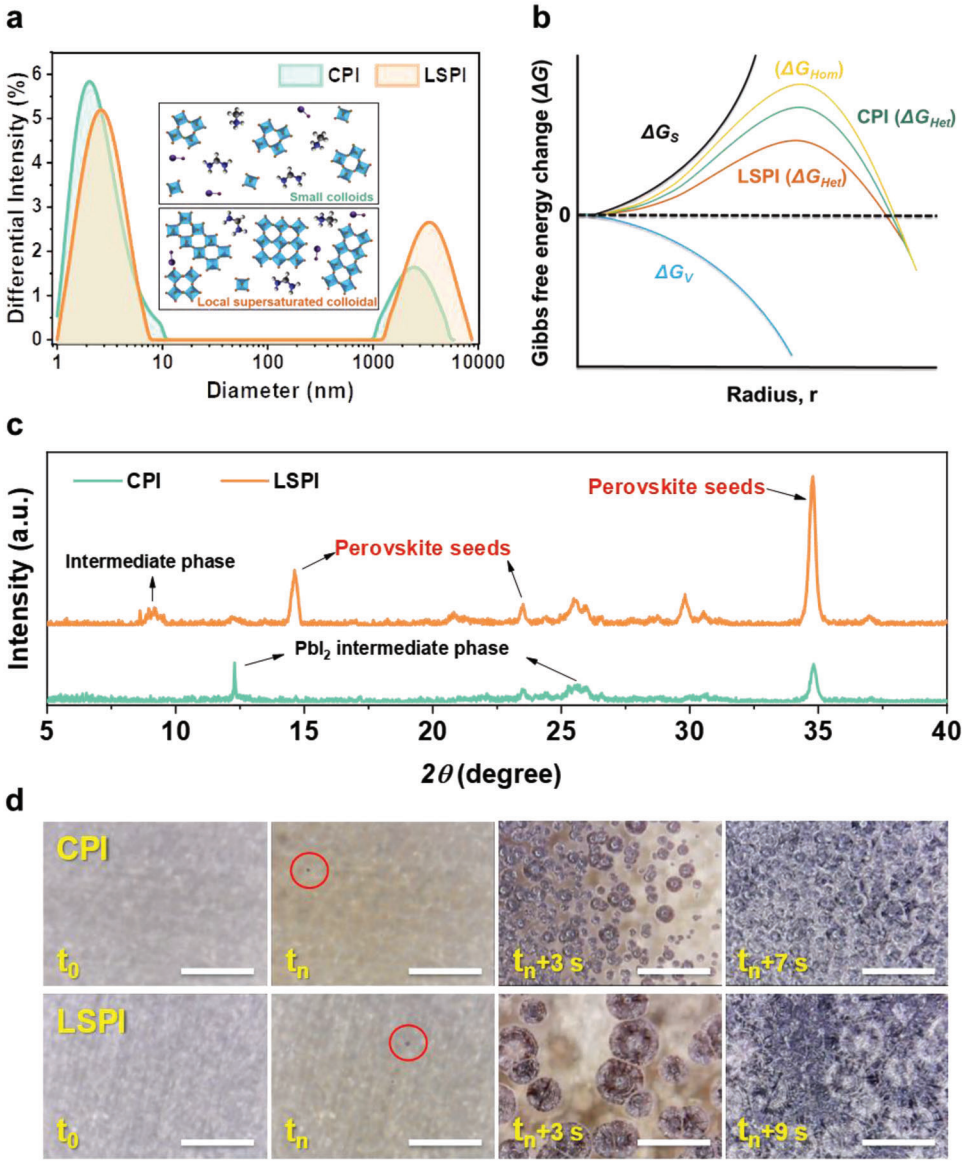

Figure 3. Nucleation and growth mechanisms of LSPI. a) Dynamic light scattering (DLS) results of the CPI and LSPI. b) The Gibbs energy change (ΔG) as a function of nuclei radius (r) based on the classical nucleation theory, where ΔG_V and ΔG_S are the volume term and surface term for Gibbs free energy, respectively. ΔG_{Hom} and ΔG_{Het} present the ΔG for homogeneous and heterogeneous nucleation, respectively. c) The X-ray diffraction (XRD) patterns of unannealed CPI and LSPI-based perovskite thin films. d) In situ optical microscopy images with a scale bar 100 μm showing the crystal growth process in CPI and LSPI-based perovskite thin films (t_0 represents the perovskite wet film state; t_n represents the initiation of nucleation and grain growth).

along with an intermediate phase (2θ = 9.1°, 12.2°, and 25.6°). In particular, the intermediate phase observed at 2θ = 9.1° in the XRD pattern of the unannealed LSPI-based perovskite thin film was confirmed to be FAI(MABr)–PbX_2–DMSO (X = I, Br), which slows down the crystallization of perovskite, allowing for a balanced control of nucleation and growth and enabling the formation of smooth and uniform perovskite films.[23] Therefore, it can be concluded that upon addition of DCB, the FAI(MABr)–PbX_2–DMSO (X = I, Br) intermediate phase is formed simultaneously with perovskite seeds (large colloids). These results are consistent with the DLS results that LSPI has coarser colloids, and it can be inferred that coarse colloids requiring low nucleation energy have grown into perovskite seeds; Coarse perovskite colloids are easily transformed into perovskite crystals without thermal annealing. The in situ optical microscopy video provided clear observation and comprehensible evidence of the crystallization kinetics and thin film formation process of the locally supersaturated perovskite ink (Videos S1 and S2, Supporting Information). As illustrated in the microscopic image over time in Figure 3d, it was observed that in CPI with small colloids, several crystals grew simultaneously to form small domains, while in LSPI with coarse colloids, fewer crystals grew simultaneously to form large domains. Moreover, it was observed that a relatively thick wet film was formed in the LSPI with coarse colloids. These results

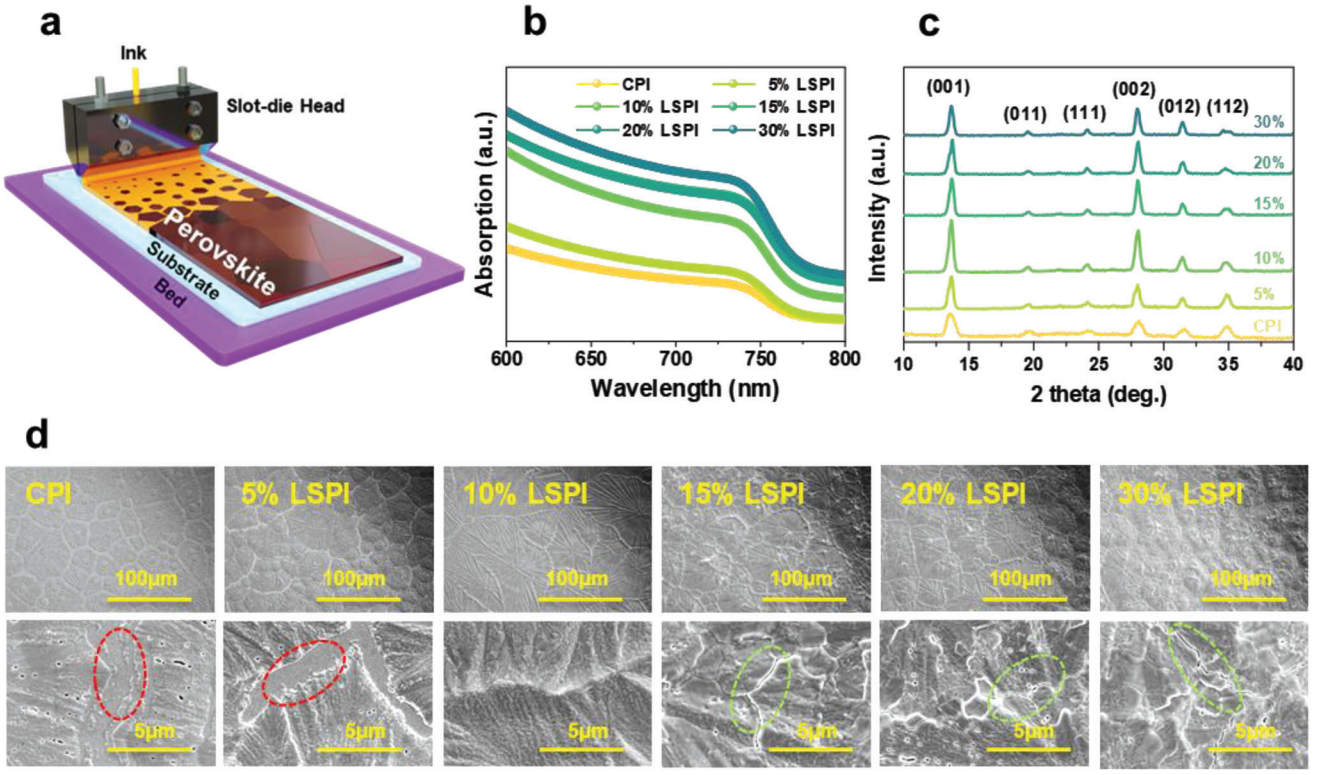

Figure 4. Slot-die process-based perovskite films. a) Schematic of slot-die coating process. b) UV–vis absorption spectra of CPI and LSPI-based perovskite thin films. c) The XRD patterns of perovskite thin films prepared by CPI and LSPI using slot-die. d) Surface morphology of CPI and LSPI-based perovskite thin films observed by field emission scanning electron microscopy (FESEM).

demonstrate that crystallization in LSPI is consistent with a heterogeneous nucleation and growth mechanism that starts from a rough colloid with low nucleation energy and rapidly grows into a crystal.

2.3. Slot-Die Process-Based Perovskite Films and Devices

The coating of the perovskite thin film was precisely controlled via a slot-die combined with a 3D printer with Z-axis resolution of 10 μm. We precisely controlled the 2D and 3D positions, feeding rate of perovskite ink, coating speed, and substrate temperature via computer software (detailed experimental procedures in the Supporting Information). All perovskite inks were used without filtering. The slot-die and the formation process of the perovskite film are illustrated in **Figure 4**a. In the case of slot-die coatings using CPI inks with high surface tension and viscosity, the ink does not transfer well from the meniscus guides to the hole transport layer and does not form a sufficiently wet film, resulting in a thin, nonuniform perovskite film.[24] By contrast, in the case of LSPI with relatively low surface tension and viscosity, the ink can transfer well from the meniscus guides to the hole transport layer and form a sufficiently wet film, resulting in a thick, uniform perovskite film.[15,20] Moreover, as described above, since the wet thin film of the perovskite precursor containing large colloids is quickly crystallized by external thermal energy,[20] a thick and uniform thin film can be formed (Figure S4, Supporting Information). The UV–vis light absorption spectrum indirectly shows that the thickness of the perovskite thin film increases with the increase of DCB addition,[25] which is consistent with the measured data using contact surface profiler (Alpha Step) (Table S3, Supporting Information). When the CPI was slot-die-coated, a very thin perovskite layer with an average thickness of 273 nm was formed, whereas in the case of LSPI with 5%, 10%, 15%, 20%, and 30% DCB, a thick perovskite layer with an average thickness of 457, 799, 880, 906, 150, and 918 nm was formed, respectively. However, unlike the change in thickness of the perovskite thin film, the optical bandgap difference between CPI and LSPI calculated by Tauc-plot was almost absent (Figure S6, Supporting Information). Additionally, XRD analysis was performed to confirm the difference in the crystal phase of the perovskite thin films coated with CPI and LSPI by slot-die (Figure 4c). In all perovskite films, typical characteristic peaks of organic–inorganic hybrid perovskite were observed; the diffraction peaks located at 13.7°, 19.6°, 24.2°, 28.0°, 31.5°, and 34.9° correspond to the (001), (011), (111), (012), and (112) crystal planes of cubic perovskite, respectively.[26] The average value of full width at half maximum showed a tendency to decrease as the amount of DCB addition increased, that is, in LSPI containing coarse colloids, indicating that crystallinity of the perovskite film improved (Table S4, Supporting Information).[26] These results indicate that there are no optical and crystallographic differences between the CPI and LSPI-based perovskite thin films except for the increase in crystallinity. However, there was a clear difference in the uniformity of perovskite thin films observed by field emission scanning electron microscope (Figure 4d). In the

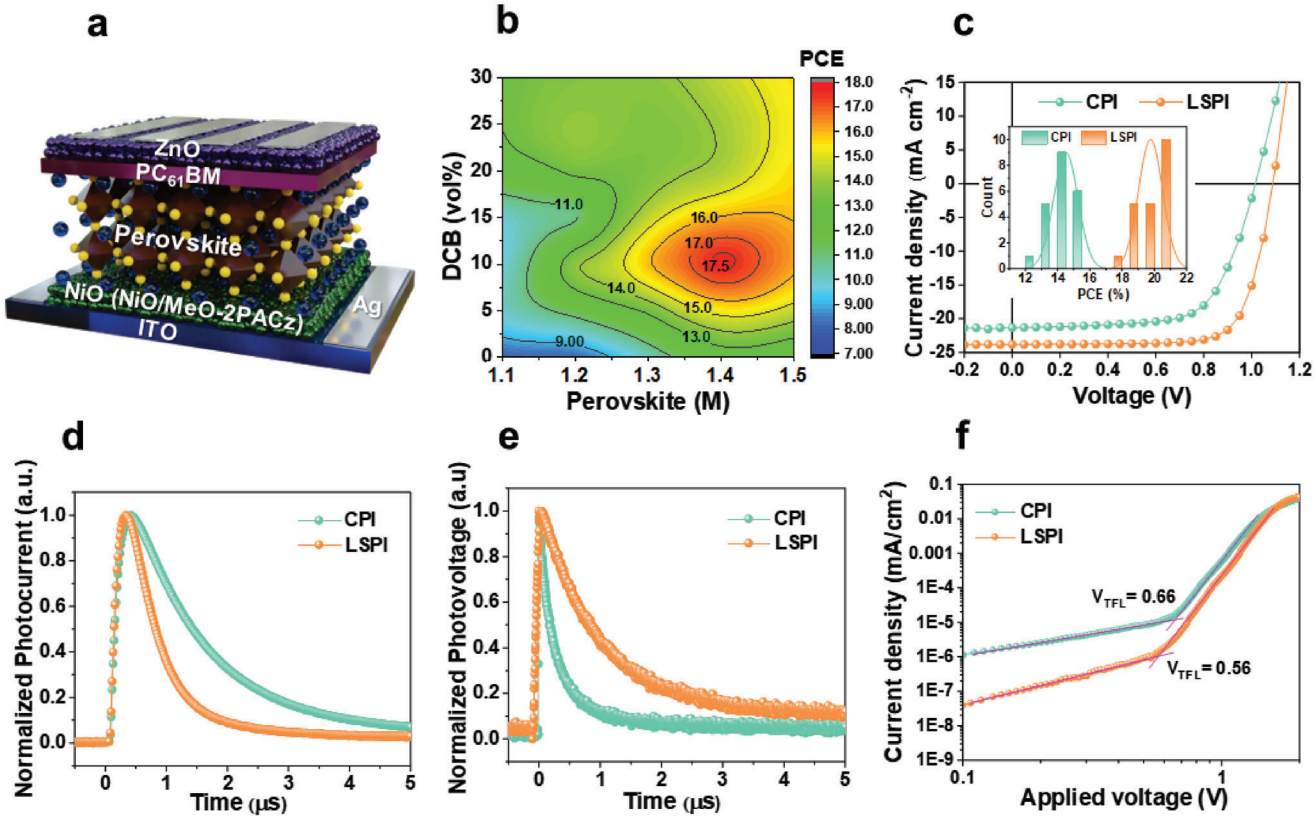

Figure 5. Slot-die process-based PSC and photovoltaics performance. a) Schematic diagram of an inverted structure (p–i–n) perovskite solar cell (PSC) with the configuration of ITO/NiO_x/perovskite/PC61BM/ZnO/Cu. b) Contour plot of PSC efficiency as a function of perovskite concentration and DCB content. c) Current–voltage (*J*–*V*) curves of the champion ITO/NiO/MeO-2PACz-based PSC with CPI and LSPI. Inset shows statistical histograms of PCEs for more than 20 corresponding devices. d) Transient photocurrent and e) transient photovoltage of the CPI and LSPI-based PSC. f) The dark *J*–*V* curves of a hole-only device consisting of ITO/NiO/perovskite/PTAA/Cu.

CPI-based perovskite thin film, it was observed that crystals grew concentrically to form small domains, irregular hollow boundaries (marked with a red circle), and pinholes. On the other hand, in the case of LSPI-based perovskite thin films containing DCB, as the amount of DCB increased, the size of the domain increased and the hollow boundary disappeared, and when 10% DCB was added, the largest domain size and a pinhole-free uniform thin film were formed. In the case of LSPI containing more DCBs, the domain became slightly smaller, and the pinhole was formed again with the crack (marked with a green circle), which is inferred from the fact that the relatively close nuclei grew rapidly, and mechanical tensile forces acted.[27] Therefore, it can be concluded that LSPI containing 10% DCB is most suitable for forming a high-quality perovskite thin film using a slot-die.

An inverted structure (p–i–n) PSC with the configuration of ITO/NiO_x/perovskite/$PC_{61}BM$/ZnO/Cu was fabricated via slot-die coating (**Figure 5**a). The coating speed and gap, which are typical process variables of slot-die coating, were systematically controlled, and the optimal process parameters were derived at a coating speed of 1.5 mm s^{-1} and a coating gap of 150 μm. (The effect of coating speed and gap on PCE in the optimization process is shown in Figure S7, Supporting Information, as a contour plot.) In addition, by analyzing the device performance correlation between various concentrations of perovskite precursors (from 1.1 to 1.5 M) and DCB (from 0 to 30 vol%) (Figure S8, Supporting Information), the optimal LSPI composition and slot-die process conditions were selected for the manufacture of high-efficiency PSCs. As a result, the optimal LSPI composition was determined as 1.4 M perovskite precursor ink containing 10 vol% DCB (Figure 5b), which was performed under the slot-die process conditions derived above. Current–voltage (*J*–*V*) curves of 1.4 M LSPI-based PSCs with DCB of various volume percentages measured under AM 1.5G illumination at 100 mW cm^{-2} are shown in Figure S9 of the Supporting Information and the corresponding photovoltaic parameters are summarized in Table S5 of the Supporting Information. The CPI-based PSC showed a relatively low PCE of 12.27%, which is due to thin film defects such as irregular hollow boundaries and pinholes that weaken solar cell performance. As 5% DCB was added, the PCE increased to 15.27%, and the highest PCE value of 17.64% with short-circuit current density (J_{SC}) of 22.92 mA cm^{-2}, open-circuit voltage (V_{OC}) of 1.09 V, and fill factor (FF) of 70.23% was obtained for the PSC with 10% LSPI (1.4 M LSPI containing 10 vol% DCB). In the case of LSPI containing DCB of 15 vol% or more, the PCE tended to decrease, which is considered to be due to the domain of the perovskite thin film becoming slightly smaller, and cracks and pinholes were formed again. Additionally, [2-(3,6 dimethoxy-9H-carbazol-9-yl) ethyl]

phosphonic acid (MeO-2PACz) self-assembled monolayer was introduced to further improve the efficiency of the PSC under optimal 10% LSPI by reducing energy loss at the NiO_x/perovskite interface.[28] Compared to the ITO/NiO-based perovskite thin film, the ITO/NiO/MeO-2PACz-based perovskite thin film exhibited a more flat and uniform morphology (Figure S10, Supporting Information), which is a beneficial for photovoltaic parameter and PSC performance.[29] PSCs with ITO/NiO/MeO-2PACz (10% LSPI) exhibited considerably higher PCE than those with ITO/NiO (Table S6, Supporting Information), with enhancement of all photovoltaic parameters. The PCE histograms of 20 devices showed the improved efficiency distribution of LPPI-based devices (average PCE 19.76%) compared to CPI-based devices (average PCE 14.50%) (inset of Figure 5c). The champion ITO/NiO/MeO-2PACz-based PSC with LSPI had a PCE of 20.61% (V_{OC} = 1.13 V, J_{SC} = 23.81 mA cm^{-2}, and FF = 76.08%) as determined from the reverse *J–V* scan and higher average PCE than those with CPI (Figure 5c). The average J_{SC} obtained from the *J–V* curves of representative PSCs was consistent with the J_{SC} obtained by integrating external quantum efficiency spectra within the error range (Figure S11, Supporting Information), indicating that the photon-to-current conversion efficiency was excellent in the LSPI-based device, resulting in improved J_{SC}. The values of series resistance (R_s) and shunt resistance (R_{sh}) for the devices CPI and LSPI are 72.32 and 18133.50 and 46.68 and 71621.11 Ω, respectively. The low R_s and high R_{sh} values in LSPI devices confirm that a large number of photogenerated charges can be more easily transported to the electrodes in LSPI devices compared to CPI, and FF can be enhanced.[30]

To examine the photoinduced charge carrier and transport dynamics in PSCs transient photocurrent (TPC) and transient photovoltage (TPV) measurements were performed under operating conditions. The estimation of TPC and TPV enables direct monitoring of the lifetime properties of photoinduced charge carriers in the solar cell as well as the assessment of time-dependent charge extraction.[31] The TPC decay times of PSCs with LSPI calculated with a biexponential decay function were 0.66 µs, which is much faster than the TPC decay times of PSCs with CPI (1.41 µs) (Figure 5d).[32] Moreover, the PSC with LSPI had a TPV decay time of 0.98 µs, whereas the PSC with CPI was shorter (0.33 µs) (Figure 5e; Tables S7 and S8, Supporting Information). These results imply that the charge carrier lifetime is extended, and the charge carrier recombination is reduced in LSPI-based PSCs.[29,33] In addition, time-resolved photoluminescence spectra (TRPL) were measured for the CPI- and LSPI-perovskite film without electron transporting layer (Figure S12, Supporting Information) and the average fluorescence lifetime (τ_w) of the perovskite film was determined by fitting the TRPL spectrum with a biexponential decay function (Table S9, Supporting Information). LSPI-perovskite film exhibited slower τ_w (≈22 ns) than CPI-perovskite film ($\tau_w \approx 14$ ns), which means that nonradiative recombination was reduced in LSPI-perovskite film, suggesting that LSPI-perovskite film has better film quality and lower defect state than CPI-perovskite film. This was confirmed by analyzing the dependence of V_{OC} on light intensity for the CPI and LSPI-based PSC (Figure S13, Supporting Information). The degree of charge carrier recombination can be derived from the slope of the semilogarithmic plot of V_{OC} versus light intensity, where the ideal factor *n* representing the degree of charge carrier recombination is derived from the slope of this linear relationship (nk_BTq^{-1}); The value of *n* theoretically converges to 1 in the absence of trap-assisted recombination in the device, so *n* values closer to 1 indicate a decrease in trap-assisted recombination.[34] Thus, the lower ideality factor of the LSPI-based PSC ($n = 1.19$) than that of the CPI-based PSC ($n = 1.93$) indicates that charge carrier recombination is significantly suppressed in LSPI-based PSCs, which coincides well with the improvement of photovoltaic parameters. Further to confirm the trap density in the CPI and LSPI-based devices, we conducted space-charge-limited current (SCLC) measurement. The SCLC measurements were performed for hole-only devices (ITO/NiO/perovskite/PTAA/Cu) by forward scanning (from 0 to 2 V) without light illumination and prebias. The trap filled limited voltage (V_{TFL}) was determined as the intersection between ($J \propto V$) Ohmic region and ($J \propto V^n$, $n > 2$) trap-filled limited region.[35] The trap density was calculated by using $N_t = 2\epsilon\epsilon_0 V_{TFL}/eL^2$ equation, where N_t is trap density, ϵ is relative dielectric constant (28.8 for perovskite), ϵ_0 is vacuum permittivity, e is the elementary charge, and L is the thickness of the perovskite film.[35,36] The V_{TFL} values of the CPI and LSPI-based hole-only devices were determined to be 0.66 and 0.56 V (Figure 5f), and the corresponding trap density values were calculated 8.40×10^{15} and 7.13×10^{15} cm^{-3}, respectively. This means that the LSPI-based perovskite thin film has a lower trap density than the CPI, and as a result, the trap-assisted charge carrier recombination in the perovskite layer is low, leading to high performance of PSC.[29,37] It can be concluded that in the PSC based on the uniform and pinhole-free LSPI-based perovskite thin film, the performance of the device is improved by reducing the trap-assisted charge carrier recombination.

2.4. Slot-Die Process-Based Modules and Stability

The minimodule was fabricated with the same layer structure as the unit cell (ITO/NiO_x/MeO-2PACz/perovskite/$PC_{61}BM$/ZnO/Cu). **Figure 6**a shows a schematic illustration of the corresponding minimodule with series-interconnections between subcells. We first performed the whole fabrication process using small area cells; A small-area minimodule was fabricated by coating a perovskite layer using slot-die with LSPI on a prepatterned (P1) ITO substrate (30 mm × 30 mm) in air (Figure S14 and Video S3, Supporting Information). The *J–V* curve of the small-area minimodule measured under AM 1.5G illumination at 100 mW cm^{-2} is shown in Figure 6b. In small-area LSPI minimodule with active area of 2.7 cm^2, the optimized parameters were able to achieve a champion PCE of 18.66% with a V_{OC} of 4.43 V, an FF of 61.17, and a J_{SC} of 6.87 mA cm^2, whereas CPI achieved only 13.29% of PCE with a V_{OC} of 4.24 V, an FF of 49.60, and a J_{SC} of 6.30 mA cm^2. This is a decrease of 9.42% compared to the PCE of the unit cell, which can be judged reasonable considering the 27-fold increase in area and the increase in series resistance. The average PCE of 20 minimodules was 17.4% (Figure 6c), and a low hysteresis index of 0.17 was shown (Figure S15, Supporting Information). Similarly, one step toward the commercial approach, a convergence minimodule (50 mm × 50 mm) combining serial and parallel interconnection. Here, a convergence minimodule was constructed based on the optimized parameters and process

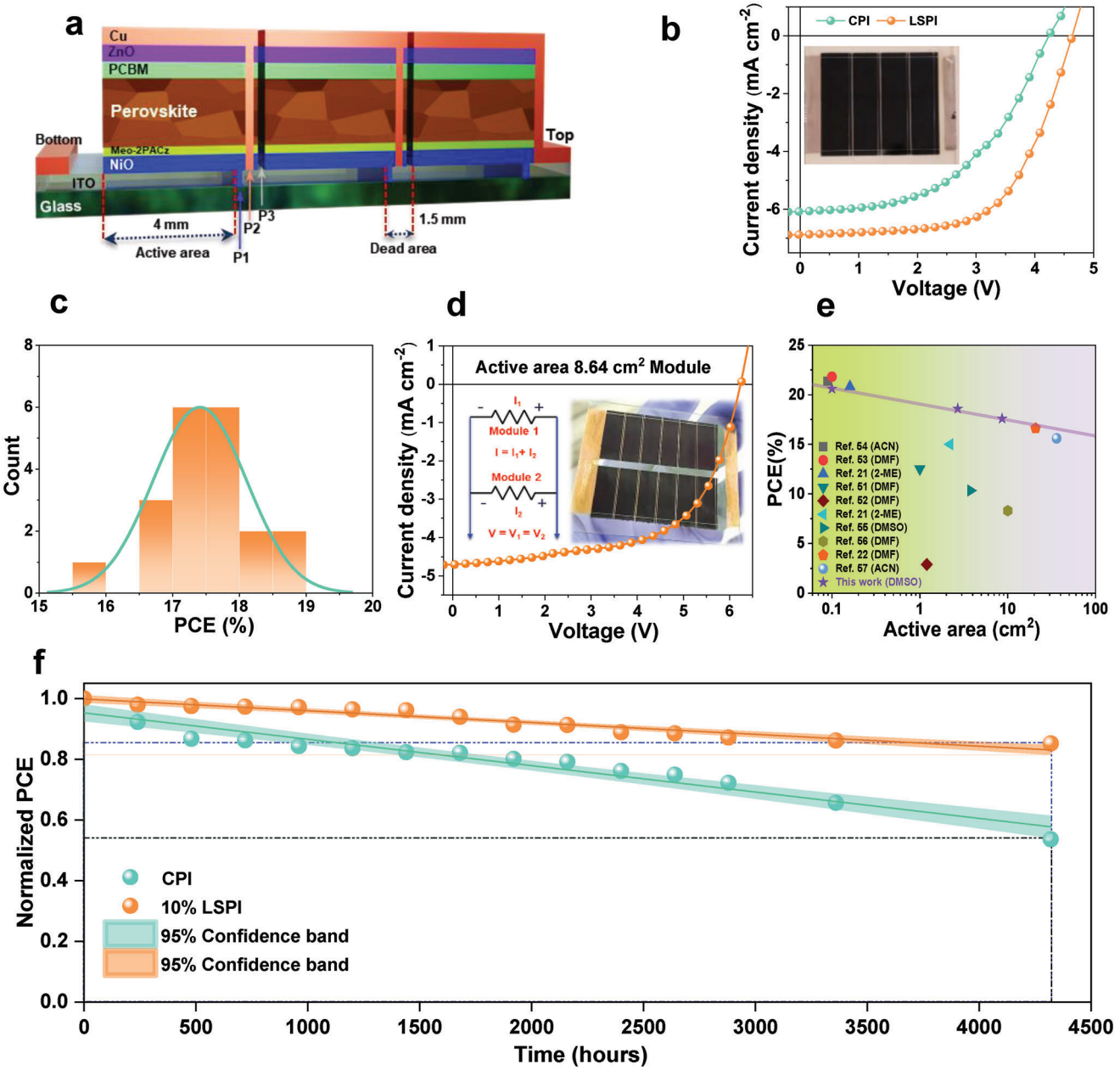

Figure 6. Slot-die process-based module and photovoltaics performance. a) Schematic architecture of minimodule with series-interconnections between subcells. b) The *J–V* curve of the small-area minimodule measured under AM 1.5G illumination at 100 mW cm^{-2}. The inset shows a corresponding small-area minimodule. c) Statistical histograms of PCEs for the corresponding 20 minimodules. d) *J–V* curves of the convergence minimodule configured by connecting the upper and lower electrodes in parallel and connecting the subcells in series. The inset shows an image of the convergence minimodule and the designed electronic circuit. e) Power conversion efficiency (PCE) of PSCs as a function of active area from this work and recent representative reports. f) The long-term stability of the unit cells based on CPI and LSPI. Unencapsulated unit cells were stored in the nitrogen environment for 4320 h.

conditions derived from the small-area minimodule. The convergence minimodule was configured by connecting the upper and lower electrodes in parallel and connecting the subcells in series (Figure 6d). This simple designed electronic circuit structure improved total photovoltaic parameters and prevented current loss in the minimodule. The convergence minimodule achieved champion PCE up to 17.66% with a V_{OC} of 6.24 V, an FF of 60.9%, and a J_{SC} of 4.70 mA cm^2 for an 8.64 cm^2 active area. Sputtering NiO_x-device results show that minimodules based on LSPI and slot-die process are competitive compared to those reported recently (Figure 6e),[12a,b,38] which presents a new route for commercialization of PSCs.

For the commercialization of PSC, not only the efficiency of the device but also the stability of the ink is very important, which is the basis for device fabrication. First, an LSPI stability test was performed by analyzing the relationship between the LSPI

storage time and the efficiency of the device. LSPI was stored in air for up to 48 h, and devices were fabricated using it. The freshly prepared LSPI showed 20.61%, and the LSPI after 12, 24, and 48 h showed PCE of 20.41%, 20.31%, and 19.35%, respectively (Figure S16, Supporting Information). These results show that LSPI can remain stable for at least 24 h, which may be suitable for use for commercialization. Finally, to test the long-term operational stability of representative unit cells and minimodules based on CPI and LSPI, unencapsulated unit cells and minimodules were stored in the nitrogen environment for 4320 h (Figure 6f) and 1920 h (Figure S17, Supporting Information). The LSPI-based unit cell maintained 85% of the PCE, and the LSPI-based minimodule maintained 83% of the PCE, while the CPI-based unit cell maintained only 53% of the PCE. Furthermore, as shown in Figure S18 of the Supporting Information, the LSPI-based device exhibited higher and more stable time-dependent current density output than the CPI devices, indicating better operational stability. In addition, the LSPI-based minimodule with encapsulation maintained 59% (while CPI retained 29%) of PCE for 200 h under 1 sun condition at ambient environment (Figure S19a, Supporting Information), and similarly maintained 59% (while CPI retained 30%) of PCE for 100 h under damp heat conditions (T_{85} and RH_{85}) (Figure S19b, Supporting Information). These results show that the unit cells and modules fabricated through the LSPI, and slot-die processes have comparatively good long-term operational stability.[12a,38c,d,f,39]

3. Conclusion

In summary, we demonstrated for the first time a rheological engineering-based LSPI strategy for a greenable slot-die process-based PSC fabrication. LSPI is formulated with low-toxic DMSO single solvent and DCB as a modulator to control the rheological properties of the ink. The DCB lowered the high surface tension of the LSPI to suit the slot-die process, enabling uniform wet film formation, and produced locally supersaturated colloids, i.e., perovskite seeds, that helped growth into dense and large domains by heterogeneous nucleation with low Gibbs-free energy. LSPI has led to the formation of high-quality perovskite thin films using a slot-die, and as a result, the LSPI enabled slot-die process-based PSCs with a PCE of 20.61% (active areas of 0.1 cm^2). In addition, LSPI also allowed minimodule with high PCEs of 18.66% (active areas of 2.7 cm^2) and 17.66% (active areas of 8.64 cm^2). The unencapsulated unit cell retains over 85% PCE for more than 4320 h, and the encapsulated minimodule retains over 83% PCE for more than 1920 h with relatively good light and thermal stability. Our findings provide strategies for designing perovskite inks and important progress toward the future commercialization of PSCs based on the greenable processes.

Supporting Information

Supporting Information is available from the Wiley Online Library or from the author.

Acknowledgements

This work was supported by the National Research Foundation of Korea (NRF) grant funded by the Korea government (MSIT) (NRF-2020R1I1A1A01051961 and NRF-2021R1A2C2010353) and the Korea Electric Power Corporation (CX72220014).

Conflict of Interest

The authors declare no conflict of interest.

Data Availability Statement

The data that support the findings of this study are available in the supplementary material of this article.

Keywords

slot-die process, green solvents, locally supersaturated ink, minimodules, perovskite solar cells, rheological engineering

Received: February 20, 2023
Revised: April 28, 2023
Published online: May 31, 2023

[1] a) Z. Zhang, Q. Sun, Y. Lu, F. Lu, X. Mu, S.-H. Wei, M. Sui, *Nat. Commun.* **2022**, *13*, 3397; b) J. J. Yoo, G. Seo, M. R. Chua, T. G. Park, Y. Lu, F. Rotermund, Y.-K. Kim, C. S. Moon, N. J. Jeon, J.-P. Correa-Baena, *Nature* **2021**, *590*, 587.

[2] a) H. Zhang, K. Darabi, N. Y. Nia, A. Krishna, P. Ahlawat, B. Guo, M. H. S. Almalki, T.-S. Su, D. Ren, V. Bolnykh, *Nat. Commun.* **2022**, *13*, 89; b) J. Fang, Z. Ding, X. Chang, J. Lu, T. Yang, J. Wen, Y. Fan, Y. Zhang, T. Luo, Y. Chen, *J. Mater. Chem. A* **2021**, *9*, 13297.

[3] a) J. Küffner, J. Hanisch, T. Wahl, J. Zillner, E. Ahlswede, M. Powalla, *ACS Appl. Energy Mater.* **2021**, *4*, 11700; b) H.-S. Yun, H. W. Kwon, M. J. Paik, S. Hong, J. Kim, E. Noh, J. Park, Y. Lee, S. Il Seok, *Nat. Energy* **2022**, *7*, 828; c) Q. Liu, W. Cai, W. Wang, H. Wang, Y. Zhong, K. Zhao, *J. Phys. Chem. Lett.* **2022**, *13*, 6503.

[4] S.-H. Huang, K.-Y. Tian, H.-C. Huang, C.-F. Li, W.-C. Chu, K.-M. Lee, Y.-C. Huang, W.-F. Su, *ACS Appl. Mater. Interfaces* **2020**, *12*, 26041.

[5] a) Y. Cui, S. Wang, L. Ding, F. Hao, *Adv. Energy Sustainability Res.* **2021**, *2*, 2000047; b) R. Vidal, J.-A. Alberola-Borràs, S. N. Habisreutinger, J.-L. Gimeno-Molina, D. T. Moore, T. H. Schloemer, I. Mora-Seró, J. J. Berry, J. M. Luther, *Nat. Sustainability* **2021**, *4*, 277.

[6] a) J. Wang, F. Di Giacomo, J. Brüls, H. Gorter, I. Katsouras, P. Groen, R. A. Janssen, R. Andriessen, Y. Galagan, *Sol. RRL* **2017**, *1*, 1700091; b) Y. Galagan, F. Di Giacomo, H. Gorter, G. Kirchner, I. de Vries, R. Andriessen, P. Groen, *Adv. Energy Mater.* **2018**, *8*, 1801935; c) M. Geppert-Rybczyńska, J. K. Lehmann, J. Safarov, A. Heintz, *J. Chem. Thermodyn.* **2013**, *62*, 104; d) Y. Deng, C. H. Van Brackle, X. Dai, J. Zhao, B. Chen, J. Huang, *Sci. Adv.* **2019**, *5*, 7537.

[7] a) O. Shargaieva, H. Näsström, J. A. Smith, D. Többens, R. Munir, E. Unger, *Mater. Adv.* **2020**, *1*, 3314; b) M. Ozaki, A. Shimazaki, M. Jung, Y. Nakaike, N. Maruyama, S. Yakumaru, A. I. Rafieh, T. Sasamori, N. Tokitoh, P. Ekanayake, *Angew. Chem., Int. Ed.* **2019**, *58*, 9389.

[8] J. E. Bishop, C. D. Read, J. A. Smith, T. J. Routledge, D. G. Lidzey, *Sci. Rep.* **2020**, *10*, 6610.

[9] F. Mathies, E. J. List-Kratochvil, E. L. Unger, *Energy Technol.* **2020**, *8*, 1900991.

[10] H. Li, C. Zuo, D. Angmo, H. Weerasinghe, M. Gao, J. Yang, *Nano-Micro Lett.* **2022**, *14*, 79.

[11] Z. Li, T. R. Klein, D. H. Kim, M. Yang, J. J. Berry, M. F. Van Hest, K. Zhu, *Nat. Rev. Mater.* **2018**, *3*, 18017.

[12] a) J. Li, J. Dagar, O. Shargaieva, M. A. Flatken, H. Köbler, M. Fenske, C. Schultz, B. Stegemann, J. Just, D. M. Többens, *Adv. Energy Mater.* **2021**, *11*, 2003460; b) Z. Yang, W. Zhang, S. Wu, H. Zhu, Z. Liu, Z. Liu, Z. Jiang, R. Chen, J. Zhou, Q. Lu, *Sci. Adv.* **2021**, *7*, 3749; c) D. S. Ham, W. J. Choi, H. Yun, M. Kim, D.-H. Yeo, S. Lee, B. J. Kim, J. H. Lee, *ACS Appl. Energy Mater.* **2021**, *4*, 7611.

[13] X. Ding, J. Liu, T. A. Harris, *AIChE J.* **2016**, *62*, 2508.

[14] Y. Deng, X. Zheng, Y. Bai, Q. Wang, J. Zhao, J. Huang, *Nat. Energy* **2018**, *3*, 560.

[15] J. Li, J. Dagar, O. Shargaieva, O. Maus, M. Remec, Q. Emery, M. Khenkin, C. Ulbrich, F. Akhundova, J. A. Márquez, *Adv. Energy Mater.* **2023**, 2203898.

[16] a) Y. Yu, S. Yang, L. Lei, Y. Liu, *Nanoscale* **2017**, *9*, 2569; b) X. Xu, Y. Sun, D. He, Z. Liang, G. Liu, S. Xu, Z. Li, L. Zhu, X. Pan, *J. Mater. Chem. C* **2021**, *9*, 208.

[17] a) G. W. Kauffman, P. C. Jurs, *J. Chem. Inf. Comput. Sci.* **2001**, *41*, 408; b) A. D. Taylor, Q. Sun, K. P. Goetz, Q. An, T. Schramm, Y. Hofstetter, M. Litterst, F. Paulus, Y. Vaynzof, *Nat. Commun.* **2021**,*12*, 1878.

[18] a) K. Yan, M. Long, T. Zhang, Z. Wei, H. Chen, S. Yang, J. Xu, *J. Am. Chem. Soc.* **2015**, *137*, 4460; b) D. Benedec, I. Oniga, F. Cuibus, B. Sevastre, G. Stiufiuc, M. Duma, D. Hanganu, C. Iacovita, R. Stiufiuc, C. M. Lucaciu, *Int. J. Nanomed.* **2018**, *13*, 1041; c) S. S. Mers, E. T. D. Kumar, V. Ganesh, *Int. J. Nanomed.* **2015**, *10*, 171.

[19] a) S. Karthika, T. Radhakrishnan, P. Kalaichelvi, *Cryst. Growth Des.* **2016**, *16*, 6663; b) L. Ke, S. Luo, X. Ren, Y. Yuan, *J. Phys. D: Appl. Phys.* **2021**, *54*, 163001.

[20] Y. Zhang, Y. Wang, X. Yang, L. Zhao, R. Su, J. Wu, D. Luo, S. Li, P. Chen, M. Yu, *Adv. Mater.* **2022**, *34*, 2107420.

[21] a) K. Liu, Q. Liang, M. Qin, D. Shen, H. Yin, Z. Ren, Y. Zhang, H. Zhang, P. W. Fong, Z. Wu, *Joule* **2020**, *4*, 2404; b) H. Choi, K. Choi, Y. Choi, T. Kim, S. Lim, T. Park, *Small Methods* **2020**, *4*, 1900569.

[22] X. Guo, C. McCleese, C. Kolodziej, A. C. Samia, Y. Zhao, C. Burda, *Dalton Trans.* **2016**, *45*, 3806.

[23] a) C. Hu, S. B. Shivarudraiah, H. H. Sung, I. D. Williams, J. E. Halpert, S. Yang, *Sol. RRL* **2021**, *5*, 2000712; b) C. Chen, Z. Zhou, Y. Jiang, Y. Feng, Y. Fang, J. Liu, M. Chen, J. Liu, J. Gao, S.-P. Feng, *ACS Appl. Mater. Interfaces* **2022**, *14*, 17348.

[24] M.-R. Ahmadian-Yazdi, A. Rahimzadeh, Z. Chouqi, Y. Miao, M. Eslamian, *AIP Adv.* **2018**, *8*, 025109.

[25] Z. Liang, S. Zhang, X. Xu, N. Wang, J. Wang, X. Wang, Z. Bi, G. Xu, N. Yuan, J. Ding, *RSC Adv.* **2015**, *5*, 60562.

[26] S. Thakur, S.-N. Kwon, D. S. Mann, S.-I. Na, *J. Materiomics* **2022**, *8*, 1165.

[27] a) F. Yang, M. A. Kamarudin, D. Hirotani, P. Zhang, G. Kapil, C. H. Ng, T. Ma, S. Hayase, *Sol. RRL* **2019**, *3*, 1800275; b) W. Qiu, T. Merckx, M. Jaysankar, C. M. De La Huerta, L. Rakocevic, W. Zhang, U. W. Paetzold, R. Gehlhaar, L. Froyen, J. Poortmans, *Energy Environ. Sci.* **2016**, *9*, 484.

[28] a) P. Patil, D. S. Mann, U. T. Nakate, Y.-B. Hahn, S.-N. Kwon, S.-I. Na, *Chem. Eng. J.* **2020**, *397*, 125504; b) D. Song, S. Narra, M.-Y. Li, J.-S. Lin, E. W.-G. Diau, *ACS Energy Lett.* **2021**, *6*, 4179; c) A. Al-Ashouri, E. Köhnen, B. Li, A. Magomedov, H. Hempel, P. Caprioglio, J. A. Márquez, A. B. Morales Vilches, E. Kasparavicius, J. A. Smith, *Science* **2020**, *370*, 1300; d) N. Phung, M. Verheijen, A. Todinova, K. Datta, M. Verhage, A. Al-Ashouri, H. Köbler, X. Li, A. Abate, S. Albrecht, *ACS Appl. Mater. Interfaces* **2021**, *14*, 2166.

[29] M.-J. Choi, Y.-S. Lee, I. H. Cho, S. S. Kim, D.-H. Kim, S.-N. Kwon, S.-I. Na, *Nano Energy* **2020**, *71*, 104639.

[30] Y. Wu, N. Ding, Y. Zhang, B. Liu, X. Zhuang, S. Liu, Z. Nie, X. Bai, B. Dong, L. Xu, *Adv. Energy Mater.* **2022**, *12*, 2200005.

[31] D. Kiermasch, P. Rieder, K. Tvingstedt, A. Baumann, V. Dyakonov, *Sci. Rep.* **2016**, *6*, 39333.

[32] W. Xu, X. Yao, T. Meng, K. Wang, F. Huang, X. Gong, Y. Cao, *J. Mater. Chem. C* **2017**, *5*, 4190.

[33] C. R. McNeill, I. Hwang, N. C. Greenham, *J. Appl. Phys.* **2009**, *106*, 024507.

[34] a) C. M. Proctor, M. Kuik, T.-Q. Nguyen, *Prog. Polym. Sci.* **2013**, *38*, 1941; b) G. J. A. Wetzelaer, M. Scheepers, A. M. Sempere, C. Momblona, J. Ávila, H. J. Bolink, *Adv. Mater.* **2015**, *27*, 1837.

[35] E. A. Duijnstee, J. M. Ball, V. M. Le Corre, L. J. A. Koster, H. J. Snaith, J. Lim, *ACS Energy Lett.* **2020**, *5*, 376.

[36] a) T. Bu, J. Li, H. Li, C. Tian, J. Su, G. Tong, L. K. Ono, C. Wang, Z. Lin, N. Chai, *Science* **2021**, *372*, 1327; b) D. S. Mann, P. Patil, S.-N. Kwon, S.-I. Na, *Appl. Surf. Sci.* **2021**, *560*, 149973; c) Y.-J. Kang, S.-N. Kwon, S.-P. Cho, Y.-H. Seo, M.-J. Choi, S.-S. Kim, S.-I. Na, *ACS Energy Lett.* **2020**, *5*, 2535.

[37] D. S. Mann, S.-N. Kwon, P. Patil, S.-I. Na, *Nano Energy* **2023**, *106*, 108062.

[38] a) Y.-S. Jung, K. Hwang, Y.-J. Heo, J.-E. Kim, D. Lee, C.-H. Lee, H.-I. Joh, J.-S. Yeo, D.-Y. Kim, *ACS Appl. Mater. Interfaces* **2017**, *9*, 27832; b) J. Ciro, M. A. Mejía-Escobar, F. Jaramillo, *Sol. Energy* **2017**, *150*, 570; c) A. S. Subbiah, F. H. Isikgor, C. T. Howells, M. De Bastiani, J. Liu, E. Aydin, F. Furlan, T. G. Allen, F. Xu, S. Zhumagali, *ACS Energy Lett.* **2020**, *5*, 3034; d) F. Xu, J. Liu, A. S. Subbiah, W. Liu, J. Kang, G. T. Harrison, X. Yang, F. H. Isikgor, E. Aydin, M. De Bastiani, *Small Sci.* **2021**, *1*, 2000044; e) S. H. Huang, C. K. Guan, P. H. Lee, H. C. Huang, C. F. Li, Y. C. Huang, W. F. Su, *Adv. Energy Mater.* **2020**, *10*, 2001567; f) D. Lee, Y.-S. Jung, Y.-J. Heo, S. Lee, K. Hwang, Y.-J. Jeon, J.-E. Kim, J. Park, G. Y. Jung, D.-Y. Kim, *ACS Appl. Mater. Interfaces* **2018**, *10*, 16133; g) E. Bi, W. Tang, H. Chen, Y. Wang, J. Barbaud, T. Wu, W. Kong, P. Tu, H. Zhu, X. Zeng, *Joule* **2019**, *3*, 2748.

[39] a) J. F. Benitez-Rodriguez, D. Chen, A. D. Scully, C. D. Easton, D. Vak, H. Li, P. E. Shaw, P. L. Burn, R. A. Caruso, M. Gao, *Sol. Energy Mater. Sol. Cells* **2022**, *246*, 111884; b) H.-J. Lee, S.-I. Na, *Mater. Lett.* **2022**, *312*, 131651.